

Supporting Information for:

**Characterization of a Proposed Terminal Iron(III) Nitride Intermediate of Nitrogen
Fixation Stabilized by a Trisphosphine-Borane Ligand**

Dirk J. Schild, Lucie Nurdin, Marc-Etienne Moret, Paul H. Oyala*, and Jonas C. Peters*

Division of Chemistry and Chemical Engineering, California Institute of Technology (Caltech),
Pasadena, California 91125, United States

Table of Contents

1. Experimental Section	2
2. NMR Spectra	10
3. IR Spectra	12
4. EPR Spectra	13
5. Mössbauer Spectra	24
6. UV-Vis Spectra	25
7. Crystallographic Details and Tables	27
8. DFT Calculations	30
9. References:	32

1. Experimental Section

General considerations. All manipulations were carried out using standard Schlenk or glovebox techniques under an N₂ atmosphere. Unless otherwise noted, solvents were deoxygenated and dried by thoroughly sparging with N₂ gas followed by passage through an activated alumina column in the solvent purification system by SG Water, USA LLC. 2-MeTHF was degassed by three freeze-pump-thaw cycles, followed by drying over NaK to remove traces of water. All reagents were purchased from commercial vendors and used without further purification unless stated otherwise. P₃^B,¹ [(P₃^B)Fe(N₂)],² [(P₃^B)Fe][BAr^F],³ and were synthesized following literature procedures. Deuterated solvents were purchased from Cambridge Isotope Laboratories, Inc., degassed, and dried over activated 3-Å molecular sieves prior to use.

¹H and ¹³C chemical shifts are reported in ppm relative to tetramethylsilane, using residual solvent proton and ¹³C resonances as internal standards. ³¹P chemical shifts are reported relative to 85 % aqueous H₃PO₄. Solution phase magnetic measurements were performed by the Evans' method.⁴

IR Spectroscopy. IR measurements were performed on a Bruker Alpha Platinum ATR spectrometer.

CW-EPR Spectroscopy. All X-band CW-EPR spectra were obtained on a Bruker (Billerica, MA, USA) EMX spectrometer. Spectra at 77 K were measured using Bruker SHQE resonator and a vacuum insulated quartz finger dewar filled with liquid nitrogen. For all 5 K CW-EPR spectra, a Bruker dual mode resonator tuned to perpendicular mode was used with an Oxford Instruments ESR900 helium flow cryostat and ITC503 temperature controller.

Pulse EPR Spectroscopy. All pulse Q-band (34 GHz) EPR, electron nuclear double resonance (ENDOR) and hyperfine sublevel correlation spectroscopy (HYSCORE) experiments were

acquired using a Bruker ELEXSYS E580 pulse EPR spectrometer equipped with a Bruker D-2 Q-band ENDOR resonator. Temperature control was achieved using an ER 4118HV-CF5-L Flexline Cryogen-Free VT cryostat manufactured by ColdEdge equipped with an Oxford Instruments Mercury ITC temperature controller.

All Q-band electron spin-echo detected EPR (ESE-EPR) field-swept spectra were acquired using the 2-pulse “Hahn-echo” sequence ($\pi/2 - \tau - \pi - \tau - \text{echo}$) where τ is a fixed delay.

Q-band Davies ENDOR spectra were acquired using the pulse sequence ($\pi - T_{RF} - \pi_{RF} - t_{RF} - \pi/2 - \tau - \pi - \tau - \text{echo}$), where T_{RF} is the delay between mw pulses and RF pulses, π_{RF} is the length of the RF pulse and the RF frequency is randomly sampled during each pulse sequence. For all ENDOR scans the same t_{RF} of 1 μs was used, all other acquisition parameters are detailed in the caption for each ENDOR figure. For ^{57}Fe ENDOR spectra, an LP-2500 low-pass RF filter (Vectronics, Starkville, MS) with a cutoff frequency of 35 MHz was attached in line with the RF amplifier and ENDOR coils to eliminate contributions from ^1H harmonics in the RF region of interest.

Q-band HYSCORE spectra were acquired using the 4-pulse sequence ($\pi/2 - \tau - \pi/2 - t_1 - \pi - t_2 - \pi/2 - \tau - \text{echo}$), where τ is a fixed delay, while t_1 and t_2 are independently incremented by Δt_1 and Δt_2 , respectively. The time domain data was baseline-corrected (third-order polynomial) to eliminate the exponential decay in the echo intensity, apodized with a Hamming window function, zero-filled to eight-fold points, and fast Fourier-transformed to yield the 2-dimensional frequency domain.

In general, the ENDOR spectrum for a given nucleus with spin $I = 1/2$ (^1H , ^{57}Fe) coupled to the $S = 1/2$ electron spin exhibits a doublet at frequencies

$$\nu_{\pm} = \left| \frac{A}{2} \pm \nu_N \right| \quad (\text{E1})$$

Where ν_N is the nuclear Larmor frequency and A is the hyperfine coupling. For nuclei with $I \geq 1$ (^{14}N , ^2H , ^{11}B), an additional splitting of the ν_{\pm} manifolds is produced by the nuclear quadrupole interaction (P)

$$\nu_{\pm, m_I} = \left| \nu_N \pm \frac{3P(2m_I - 1)}{2} \right| \quad (\text{E2})$$

In HYSCORE spectra, these signals manifest as cross-peaks or ridges in the 2-D frequency spectrum which are generally symmetric about the diagonal of a given quadrant. This technique allows hyperfine levels corresponding to the same electron-nuclear submanifold to be differentiated, as well as separating features from hyperfine couplings in the weak-coupling regime ($|A| < 2|\nu_I|$) in the (+,+) quadrant from those in the strong coupling regime ($|A| > 2|\nu_I|$) in the (-,+) quadrant. The (-,-) and (+,-) quadrants of these frequency spectra are symmetric to the (+,+) and (-,+) quadrants, thus typically only two of the quadrants are typically displayed in literature. For systems with appreciable hyperfine anisotropy in frozen solutions or solids, HYSCORE spectra typically do not exhibit sharp cross peaks, but show ridges that represent the sum of cross peaks from selected orientations at the magnetic field position at which the spectrum is collected. The length and curvature of these correlation ridges allow for the separation and estimation of the magnitude of the isotropic and dipolar components of the hyperfine tensor, as shown in Figure S1.

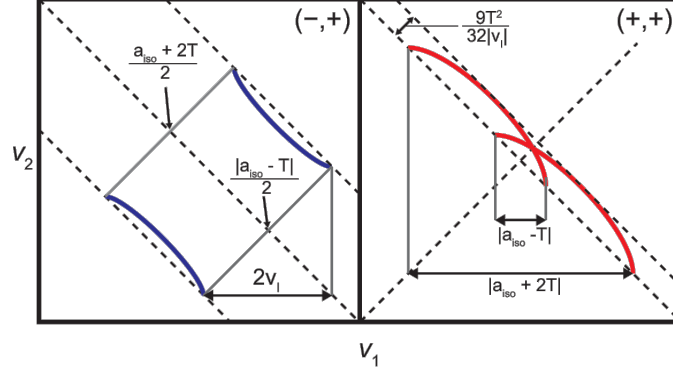


Figure S1. HYSORE powder patterns for an $S = 1/2$, $I = 1/2$ spin system with an axial hyperfine tensor which contains isotropic (a_{iso}) and dipolar (T) contributions. Blue correlation ridges represent the strong coupling case; red correlation ridges represent the weak coupling case.

For weakly coupled nuclei ($A < 2v_I$), v_α and v_β are both positive, appearing in the (+,+) quadrant, while for strongly coupled nuclei they will show up in the (-,+) quadrant. In the intermediate coupling regime where $A \approx 2v_I$, peaks will often appear in both the (+,+) and (-,+) quadrants of the HYSORE spectrum.

All EPR spectra (CW, ENDOR, HYSORE) were simulated using the EasySpin⁵ simulation toolbox (version 5.2.33) with Matlab 2020b using the following Hamiltonian:

$$\hat{H} = \mu_B \vec{B}_0 g \hat{S} + \mu_N g_N \vec{B}_0 \hat{I} + h \hat{S} \cdot \mathbf{A} \cdot \hat{I} + h \hat{I} \cdot \mathbf{P} \cdot \hat{I} \quad (\text{E3})$$

In this expression, the first term corresponds to the electron Zeeman interaction term where μ_B is the Bohr magneton, g is the electron spin g -value matrix with principal components $g = [g_{xx}, g_{yy}, g_{zz}]$, and \hat{S} is the electron spin operator; the second term corresponds to the nuclear Zeeman interaction term where μ_N is the nuclear magneton, g_N is the characteristic nuclear g -value for each nucleus (e.g. ^1H , ^2H , ^{31}P) and \hat{I} is the nuclear spin operator; the third term corresponds to the electron-nuclear hyperfine term, where \mathbf{A} is the hyperfine coupling tensor with principal

components $\mathbf{A} = [A_{xx} \ A_{yy} \ A_{zz}]$; and for nuclei with $I \geq 1$, the final term corresponds to the nuclear quadrupole (NQI) term which arises from the interaction of the nuclear quadrupole moment with the local electric field gradient (efg) at the nucleus, where \mathbf{P} is the quadrupole coupling tensor. In the principal axis system (PAS), \mathbf{P} is traceless and parametrized by the quadrupole coupling constant e^2Qq/h and the electric field gradient asymmetry parameter η such that:

$$\mathbf{P} = \begin{pmatrix} P_{xx} & 0 & 0 \\ 0 & P_{yy} & 0 \\ 0 & 0 & P_{zz} \end{pmatrix} = \frac{e^2Qq/h}{4I(2I-1)} \begin{pmatrix} -(1-\eta) & 0 & 0 \\ 0 & -(1+\eta) & 0 \\ 0 & 0 & 2 \end{pmatrix} \quad (\text{E4})$$

Where $\frac{e^2Qq}{h} = 2I(2I-1)P_{zz}$ and $\eta = \frac{P_{xx}-P_{yy}}{P_{zz}}$. The asymmetry parameter may have values between 0 and 1, with 0 corresponding to an electric field gradient with axial symmetry and 1 corresponding to a fully rhombic efg.

The orientations between the hyperfine and NQI tensor principal axis systems and the g-matrix reference frame are defined by the Euler angles (α, β, γ) , with rotations performed within the zyz convention where α rotates xyz counterclockwise about z-axis to give x'y'z', β rotates x'y'z' counterclockwise about y'-axis to give x'',y'',z'', γ rotates x''y''z'' counterclockwise about z''-axis to give final frame orientation.

Mössbauer Spectroscopy. Spectra were recorded on a spectrometer from SEE Co. operating in the constant acceleration mode in a transmission geometry. Spectra were recorded with the temperature of the sample maintained at 80 K. The sample was kept in an SVT-400 Dewar from Janis. The quoted isomer shifts are relative to the centroid of the spectrum of a metallic foil of α -Fe at room temperature. Data analysis was performed using the program WMOSS (www.wmoss.org) and quadrupole doublets were fit to Lorentzian lineshapes.

X-Ray Crystallography. X-ray diffraction studies were carried out at the Caltech Division of Chemistry and Chemical Engineering X-ray Crystallography Facility on a Bruker three-circle SMART diffractometer with a SMART 1K CCD detector, APEX CCD detector, or Bruker D8 VENTURE Kappa Duo PHOTON 100 CMOS detector. Data were collected at 100 K using Mo K α radiation ($\lambda = 0.71073 \text{ \AA}$) or Cu K α radiation ($\lambda = 1.54178 \text{ \AA}$). Structures were solved by direct or Patterson methods using SHELXS and refined against F² on all data by full-matrix least squares with SHELXL-97.68 All non-hydrogen atoms were refined anisotropically. All hydrogen atoms were placed at geometrically calculated positions and refined using a riding model. The isotropic displacement parameters of all hydrogen atoms were fixed at 1.2 (1.5 for methyl groups) times the U_{eq} of the atoms to which they are bonded.

[(P₃^B)Fe(Cl)] (1). A mixture of FeCl₂ (87 mg, 0.69 mmol), P₃^B (400 mg, 0.69 mmol), iron powder (415 mg, 7.4 mmol), and THF (20 mL) was heated to 90 °C in a sealed bomb under vigorous stirring for 62 h, during which time the color of the liquid phase turned from pale yellow to brown. The remaining iron powder was removed by filtration, and the solvent was removed *in vacuo*. The brown residue was taken in toluene (10 mL) and dried *in vacuo*. The brown residue was extracted with pentane (200 mL) to give a brown solution. Solvent evaporation *in vacuo* afforded the product as a greenish-brown powder (422 mg, 90%). An analytically pure sample was obtained by slow concentration of a saturated pentane solution. Crystals suitable for XRD were obtained upon cooling a saturated solution of (P₃^B)Fe(Cl) in pentane to -35 °C. ¹H NMR (C₆D₆, 300 MHz): δ 96.9 (1H), 35.0 (1H), 23.6 (1H), 9.8(1H), 5.8 (1H), 1.9 (3H), -0.3 (3H), -2.3 (3H), -22.4 (1H). UV-vis (THF, nm {cm⁻¹ M⁻¹}): 280 {2.0·10⁴}, 320 {sh}, 560 {sh}, 790 {150}, 960 {190}. μ_{eff} (C₆D₆, Evans method, 20 °C): 4.0 μ_{B} . Anal: calcd for C₃₆H₅₄BClFeP₃: C 63.41, H 7.98; found: C 63.16, H 7.72.

[(P₃^B)Fe(N₃)] (2). A mixture of **1** (100 mg, 0.15 mmol) and sodium azide (15 mg, 0.23 mmol) in THF (3 mL) was stirred for 10 days at room temperature. The solvent was removed *in vacuo* and the solid residue was extracted with benzene. Lyophilization afforded the product as a brown powder (100 mg, 99%). Crystals suitable for XRD were obtained upon cooling a saturated solution of **(P₃^B)Fe(N₃)** in pentane to -35 °C. ¹H NMR (C₆D₆, 300 MHz): δ 72.5 (3H), 34.3 (3H), 23.0 (3H), 12.3 (3H), 5.9 (3H), 1.7 (9H), 1.1 (9H), 0.5 (9H), -1.8 (9H), -21.5 (3H). UV-vis (DEE, nm {cm⁻¹ M⁻¹}): 280 {sh}, 340 {sh}, 370 {1.1·10⁴}, 600 {sh}, 820 {160}, 1000{190}. μ_{eff} (C₆D₆, Evans method, 20 °C): 3.8 μ_B. IR (ATR, THF film): ν_{NNN} = 2069 cm⁻¹. Anal: calcd for C₃₆H₅₄BF₃FeN₃P₃: C 62.81, H 7.91, N 6.10; found: C 63.26, H 7.65, N 6.09.

[(P₃^B)Fe(N*NN*) (N*: 50% ¹⁵N (2-¹⁵N))] was prepared as **2** using Na¹⁵NNN. ν_{NNN} = 2058 cm⁻¹.

[(P₃^B)⁵⁷Fe(N₃)] (2-⁵⁷Fe) was prepared as **2** using (P₃^B)⁵⁷Fe(Cl).

[(P₃^B)₂(μ-1,3-N₃)] (3) A brown solution of (P₃^B)Fe(N₂) (20 mg, 30 μmol) in benzene (1 mL) was layered on top of a brown solution of **2** (20 mg, 29 μmol) in benzene (1 mL) and left standing for 2 days. Filtration, washing with benzene (2 × 1 mL) and pentane (2 × 1 mL) followed by drying *in vacuo* afforded the product as a dark brown powder (29 mg, 76%). Crystals suitable for XRD were obtained via generating **3** in solution from equimolar amounts of **2** and (P₃^B)Fe(N₂). ¹H NMR (C₆D₆, 300 MHz): δ 47.0, 46.0 (sh), 39.3, 19.6, 12.0, 11.0 (sh), 4.3, 3.3, 2.1, 0.2, -1.8, -3.4, -7.2, -8.0. UV-vis (THF, nm {cm⁻¹M⁻¹}): 640 {sh}, 750 {sh}, 1000{sh}. NIR (THF, cm⁻¹{cm⁻¹M⁻¹}): 5250 {2.2 ·10³} (IVCT). IR (ATR, THF film): ν_{NNN} = 2090 cm⁻¹. Anal: calcd for C₇₂H₁₀₈B₂Fe₂N₃P₆: C 64.79, H 8.16, N 3.15; found: C 64.39, H 7.81, N 3.18.

Typical procedure for the photolysis of (P₃^B)Fe(N₃) at 77 K for an EPR sample.

In a nitrogen-filled glovebox, 250 μL of a 1 mM solution of $(\text{P}_3^{\text{B}})\text{Fe}(\text{N}_3)$ in 2-MeTHF were introduced in an EPR tube and frozen. The frozen tubes, in which a yellow glass was present, were taken out of the glovebox into liquid nitrogen. The sample was then irradiated with a 365 nm 40 W mercury lamp, while immersed in liquid nitrogen (see picture below). The highest conversions are observed between 5 and 10 minutes.



Typical procedure for the photolysis of $(\text{P}_3^{\text{B}})\text{Fe}(\text{N}_3)$ at 77 K for a Mössbauer sample.

In a nitrogen filled glovebox, 0.5 mL of a 1 mM solution of $(\text{P}_3^{\text{B}})^{57}\text{Fe}(\text{N}_3)$ in 2-MeTHF was introduced into a Mössbauer cup without a bottom. Transparent Kapton tape was used to cover the bottom. The cup was frozen in the glovebox and taken out and put directly into liquid nitrogen after which the tape was removed with the sample immersed in liquid nitrogen. Subsequently, the sample was irradiated with a 100 W mercury lamp. After 30 minutes, the cup was turned upside down to ensure full photolysis.

2. NMR Spectra

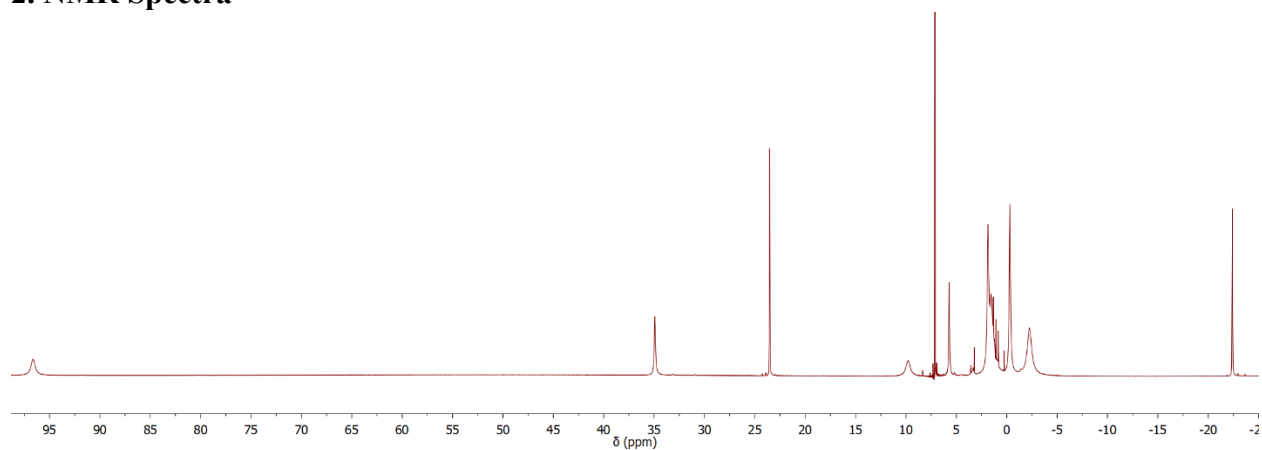


Figure S2. ¹H NMR spectrum of (P₃^B)Fe(Cl) **1** in C₆D₆

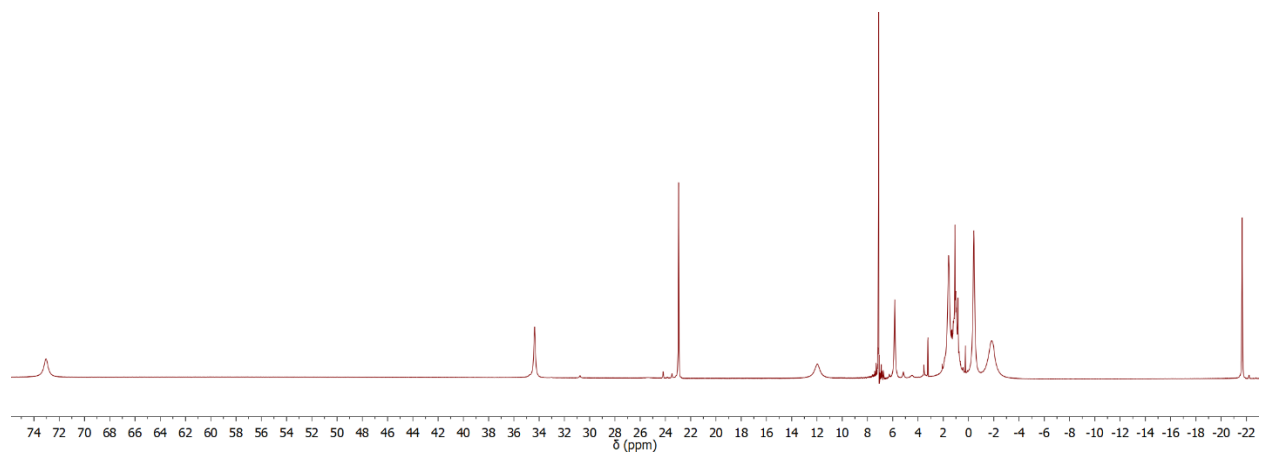


Figure S3. ¹H NMR spectrum of (P₃^B)Fe(N₃) **2** in C₆D₆

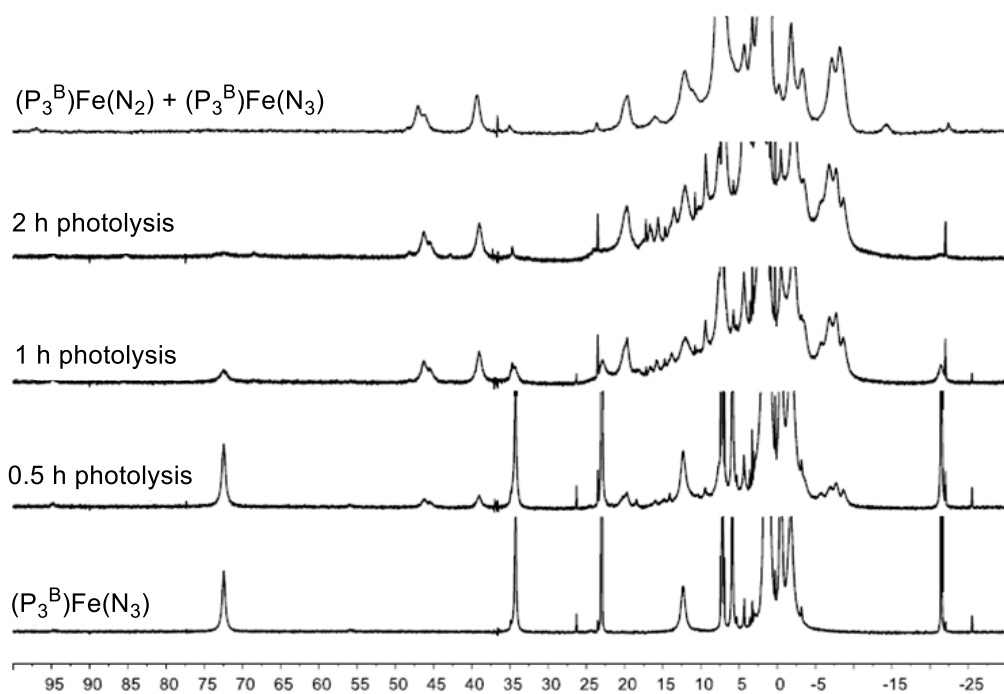


Figure S4. 1H NMR spectra monitoring the photolysis of $(P_3^B)Fe(N_3)$ (**2**) in C_6D_6 at room temperature and 1H NMR spectrum of $[(P_3^B)]_2(\mu-1,3-N_3)$ (**3**) generated *in situ* by reaction of **2** and $(P_3^B)Fe(N_2)$ recorded before complete precipitation of insoluble **3**.

3. IR Spectra

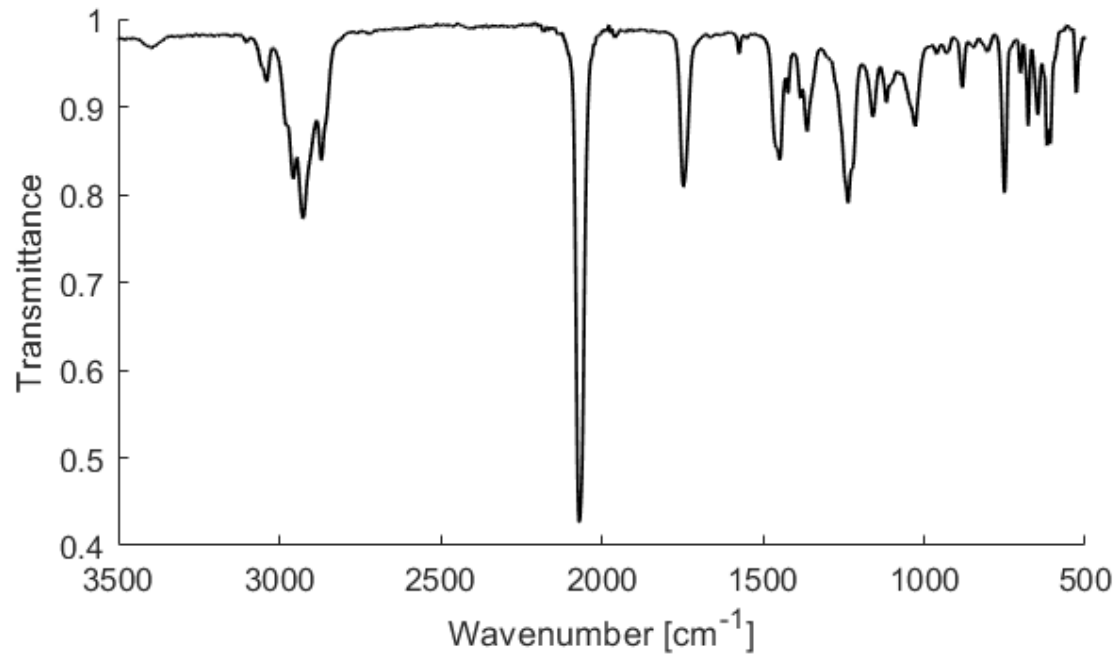


Figure S5. IR spectrum of $(P_3^B)Fe(N_3)$ (**2**) (thin-film from C_6D_6 solution)

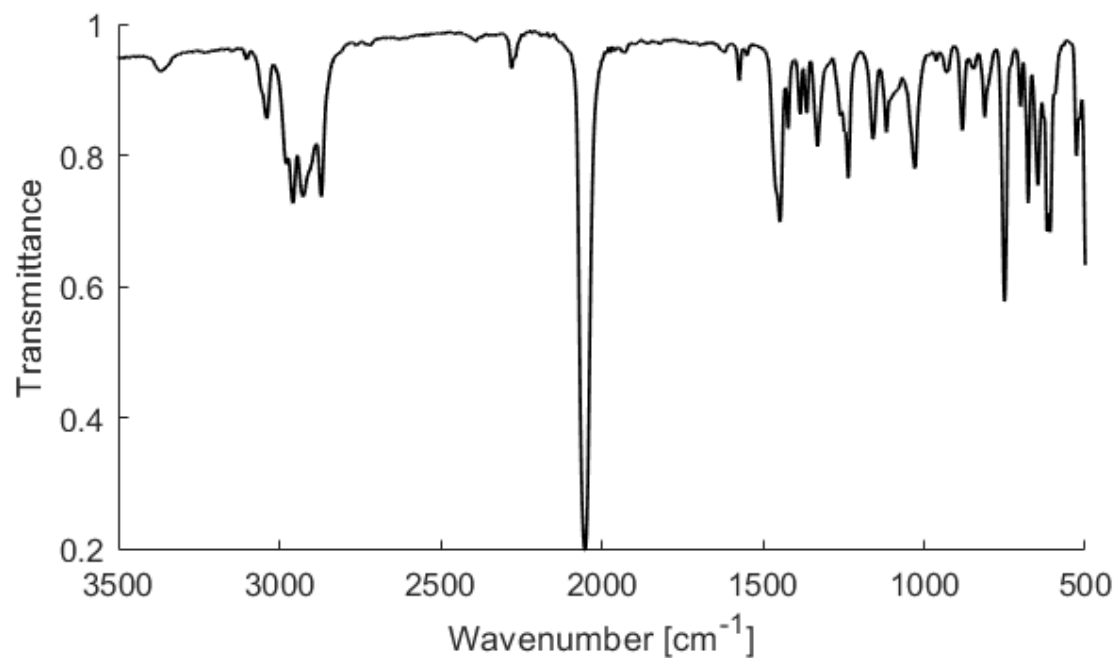


Figure S6. IR spectrum of $(P_3^B)Fe(^{15}N_3)$ (**2-¹⁵N**) (thin-film from C_6D_6 solution)

4. EPR Spectra

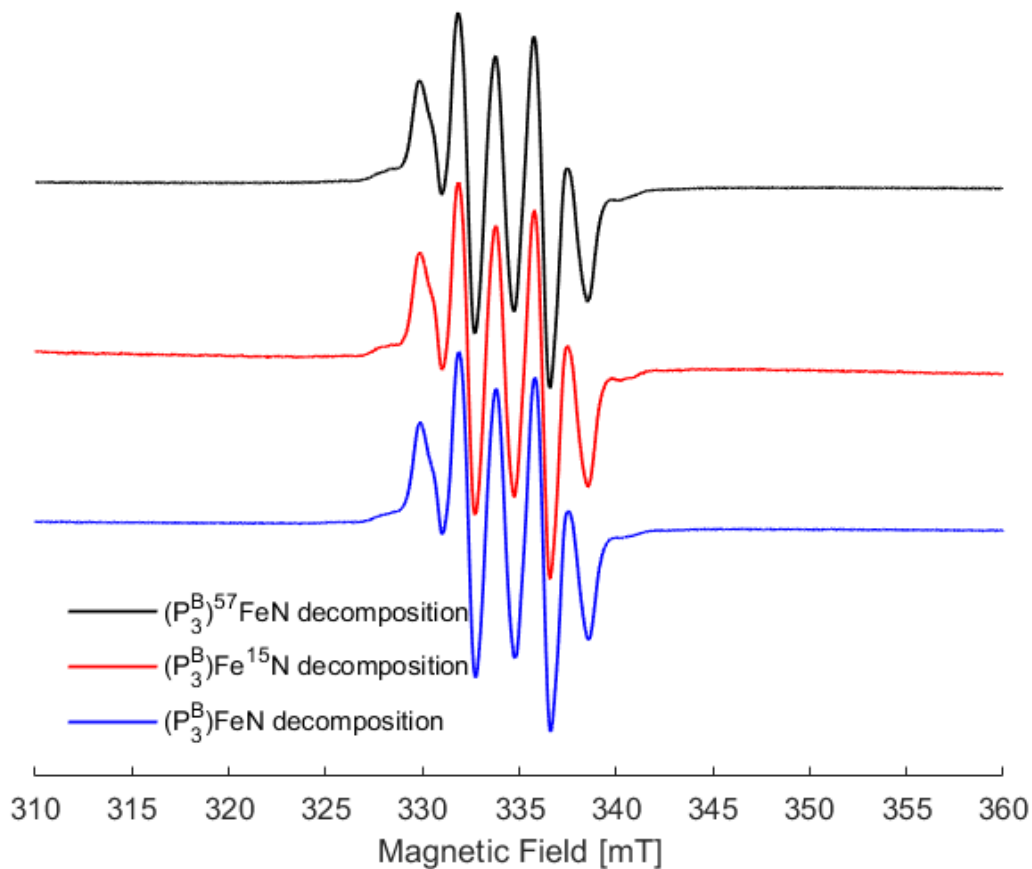


Figure S7. EPR spectra recorded after irradiating a frozen 1 mM solution of **2**, $2\text{-}^{15}\text{N}$, and $2\text{-}^{57}\text{Fe}$, showcasing the absence of isotope effects on the signal and the absence of a signal corresponding to $(\text{P}_3^{\text{B}})\text{Fe}\equiv\text{N}$ (**4**). The observed signal is identical to *i*-Pr radical.⁵ MW frequency = 9.371-9.375 GHz; temperature = 77 K; MW power = 140 μW ; modulation amplitude = 0.1 mT; conversion time = 10.24 ms.

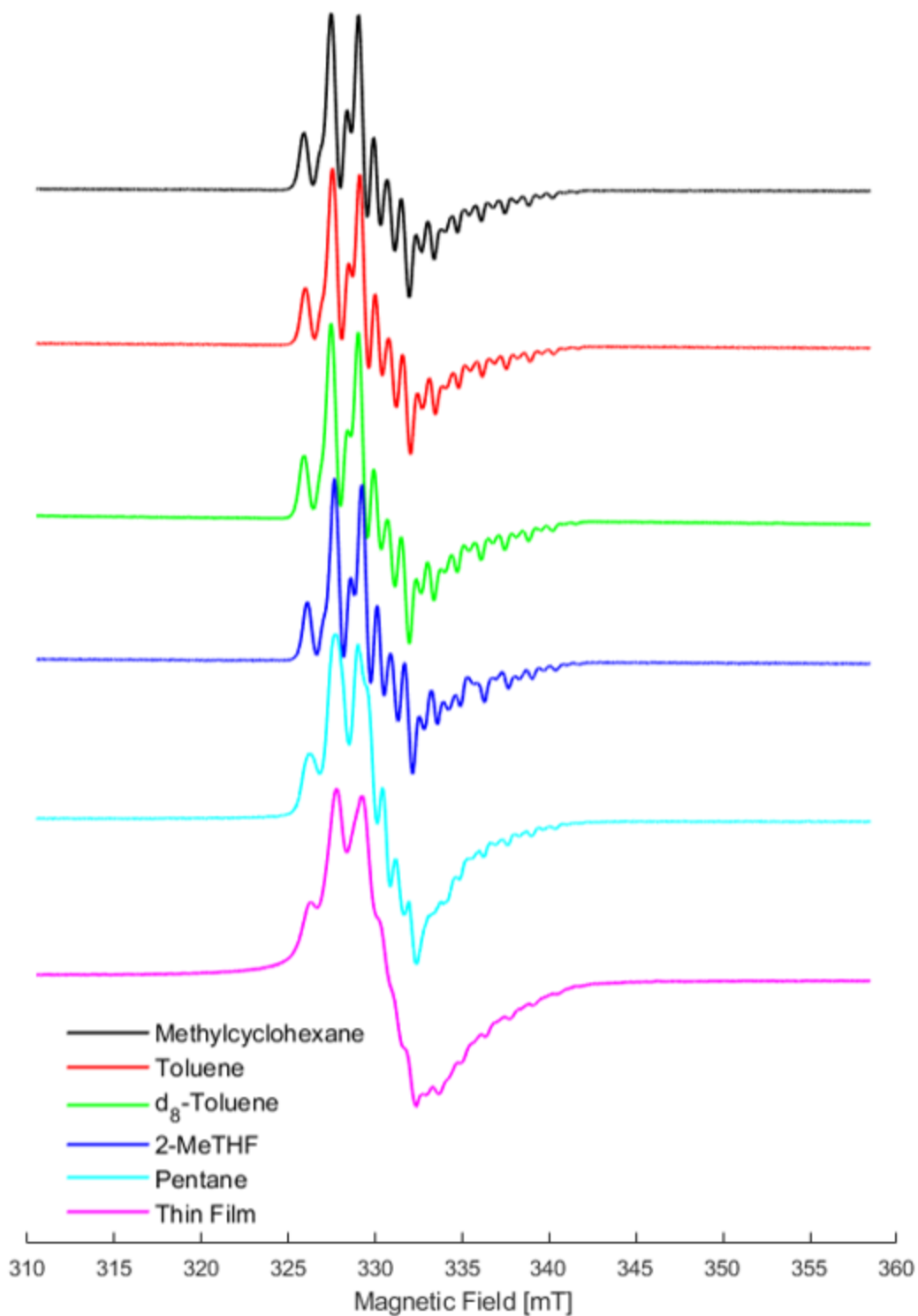


Figure S8. EPR spectra recorded after irradiating a frozen 1 mM solution of **2** in methylcyclohexane, toluene, d_8 -toluene, 2-MeTHF, pentane and as thin films deposited from pentane solutions. MW frequency = 9.371-9.375 GHz; temperature = 77 K; MW power = 140 μ W; modulation amplitude = 0.1 mT; conversion time = 10.24 ms.

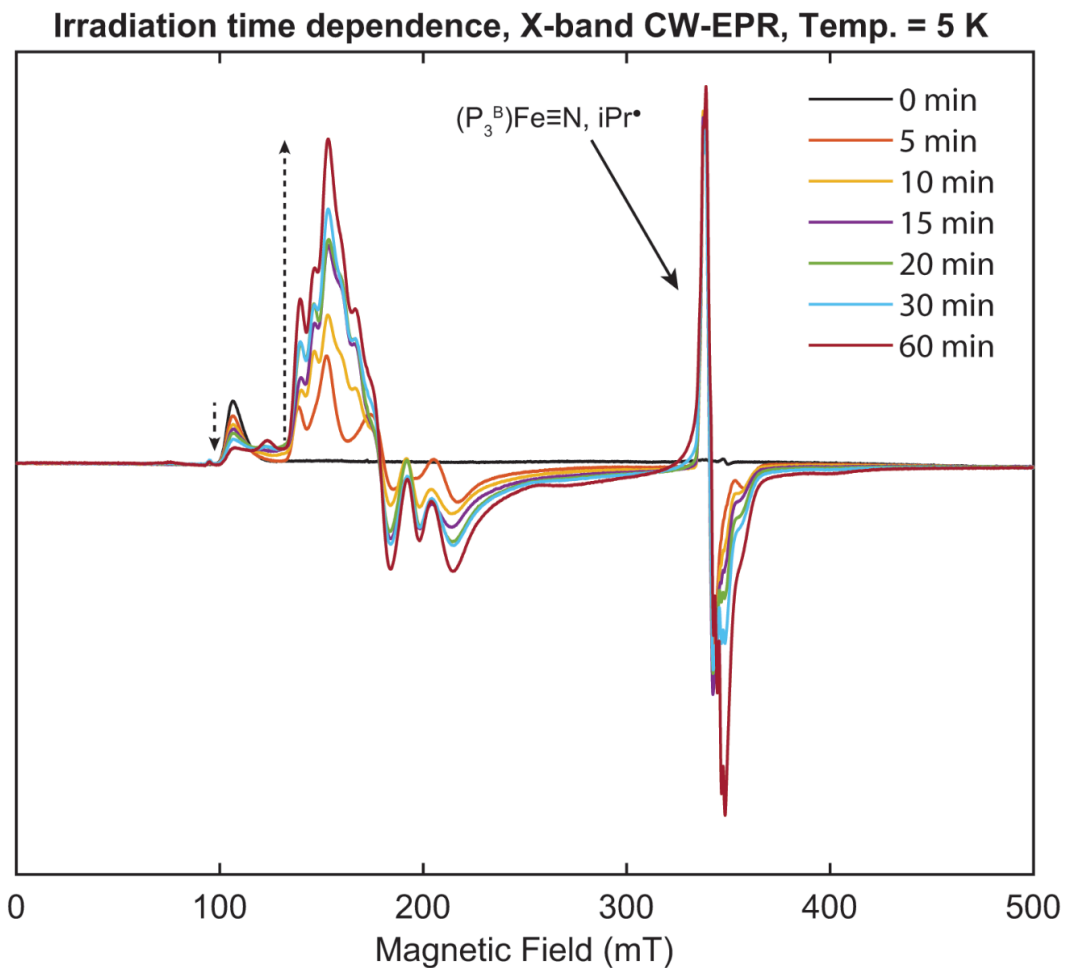


Figure S9. X-band CW-EPR-monitored photolysis of **2** in a frozen 4 mM 2-MeTHF solution at 5 K showing the decline in **2** (positive feature at ~ 110 mT) and increase in other $S = 3/2$ species (140-300 mT) during photolysis. Irradiation was conducted at 77 K in liquid nitrogen and the sample was re-measured after each irradiation interval. Sharp signals near 350 mT correspond to **4** and, at later time points, *iPr* radical. Acquisition parameters: MW frequency = 9.635-9.638 GHz; temperature = 5 K; MW power = 2.2 mW; modulation amplitude = 0.8 mT; conversion time = 10.24 ms.

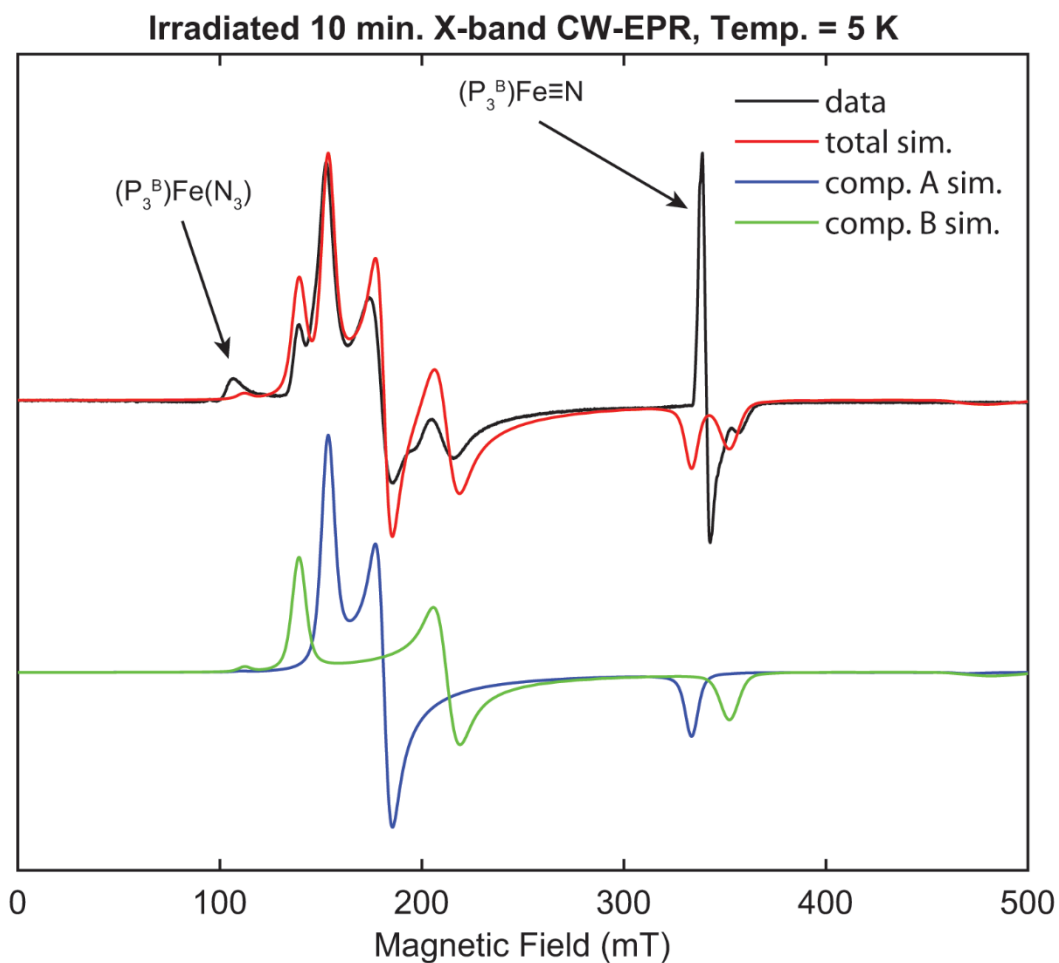


Figure S10. X-band CW-EPR spectrum at 5 K in of a frozen 2 mM solution of **2** in 2-MeTHF irradiated for 10 mins. This EPR spectrum showcases the two high-spin species that are formed concomitantly with **4**.

Acquisition parameters: MW frequency = 9.636 GHz; temperature = 5 K; MW power = 2.2 mW; modulation amplitude = 0.8 mT; conversion time = 10.24 ms.

Simulation Parameters: component A: $S = 3/2$, $g = 2.085$, $D = 1 \text{ cm}^{-1}$, $E/D = 0.055$, simulation weight = 0.6; component B: $S = 3/2$, $g = 2.085$, $D = 1 \text{ cm}^{-1}$, $E/D = 0.14$, simulation weight = 0.4.

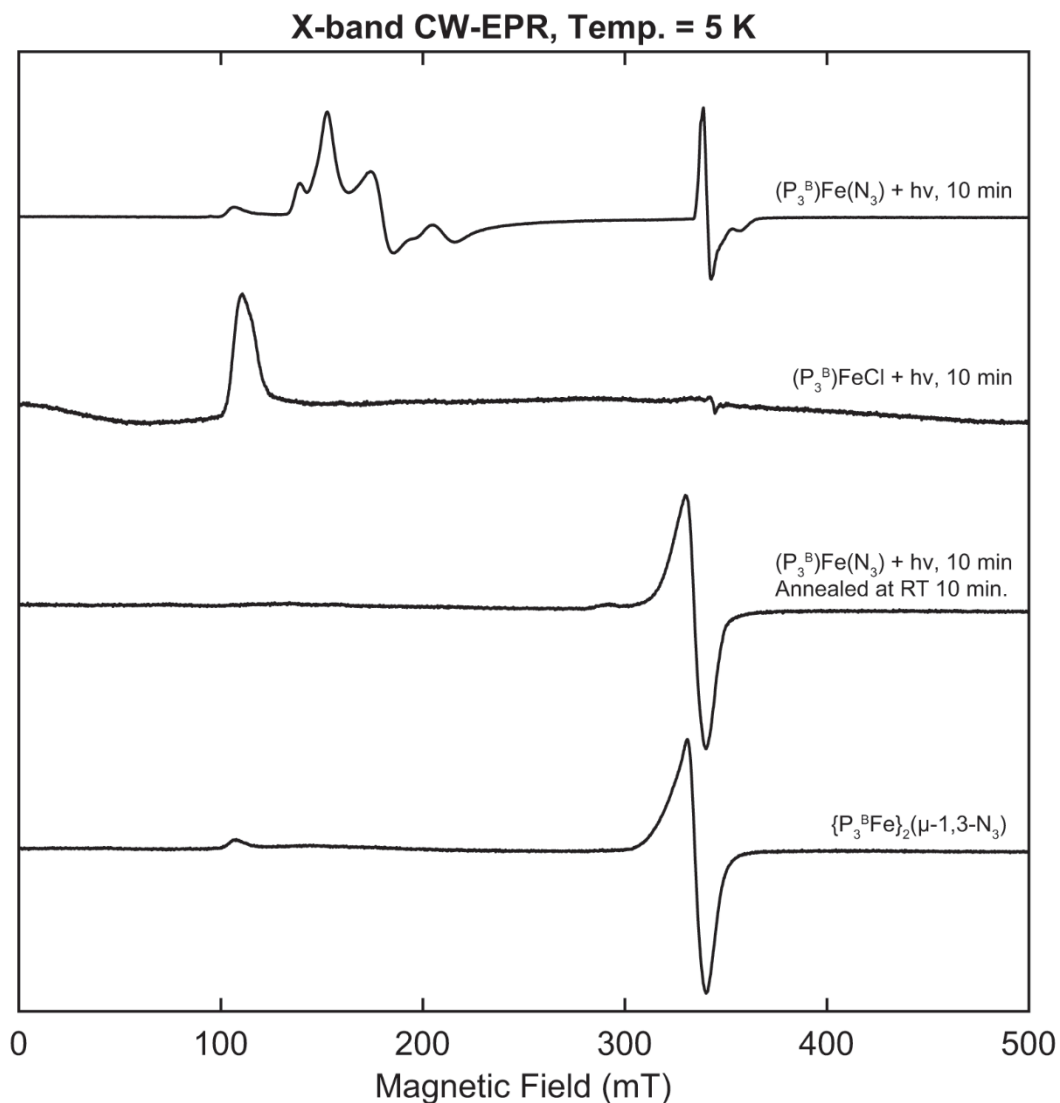


Figure S11. X-band CW-EPR spectra of frozen 2 mM solutions in 2-MeTHF of: (top) complex **2** ($P_3^BFe(N_3)$) irradiated for 10 mins; (second from top) complex **1** ($P_3^BFe(Cl)$) irradiated for 10 mins; (third from top) complex **2** ($P_3^BFe(N_3)$) irradiated for 10 mins and subsequently annealed at room temperature for 10 minutes; (bottom) complex **3** ($\{P_3^BFe\}_2(\mu-1,3-N_3)$). These experiments demonstrate that the two high spin species that are formed concomitantly with **4** are not due to ligand decomposition on its own and cannot be attributed to complex **3**, and that these signals disappear upon warming to room temperature and only a signal consistent with $\{P_3^BFe\}_2(\mu-1,3-N_3)$ is observed. Acquisition parameters: MW frequency = 9.635-9.638 GHz; temperature = 5 K; MW power = 2.2 mW; modulation amplitude = 0.8 mT; conversion time = 10.24 ms.

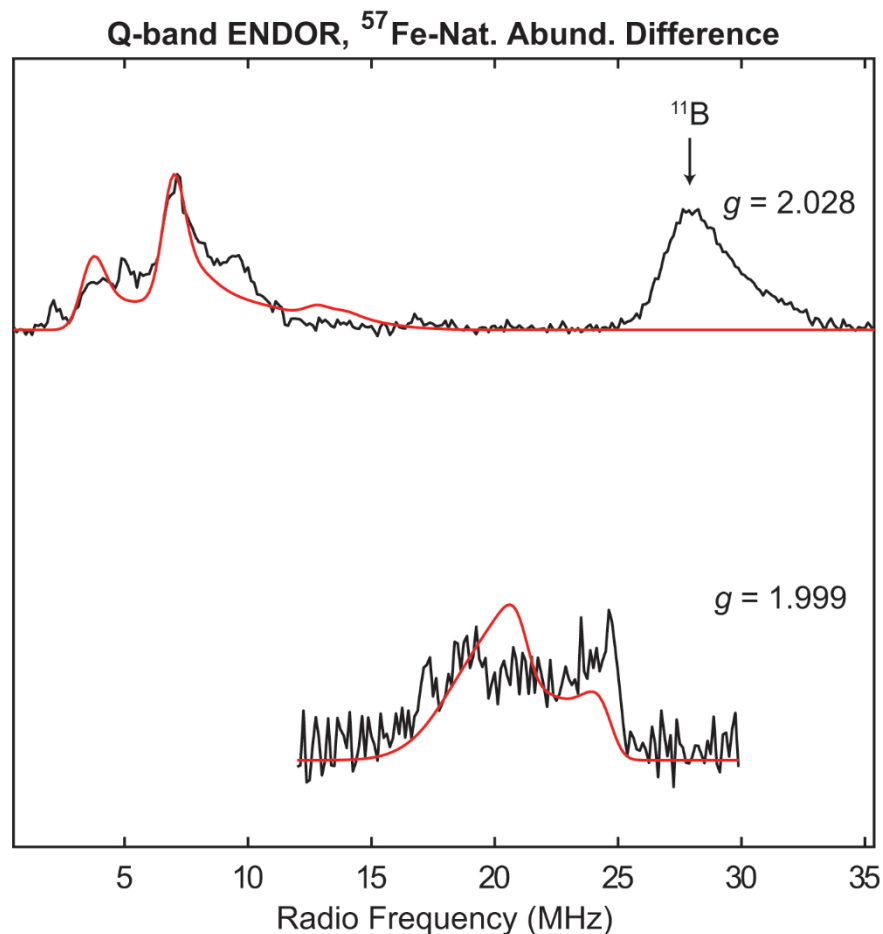


Figure S12. Field-Dependent Q-band Davies ENDOR ^{57}Fe -minus-Natural abundance difference spectra (black) of $(\text{P}_3^{\text{B}})\text{Fe}(\text{N})$ **4** with spectral simulations of contributions from ^{57}Fe overlaid using parameters in Table 1 in the main text. MW frequency = 34.103 GHz; temperature = 20 K; MW π pulse length = 160 ns; interpulse delay τ = 300 ns; π_{RF} pulse length = 40 μs ; T_{RF} delay = 2 μs ; shot repetition time (srt) = 5 ms.

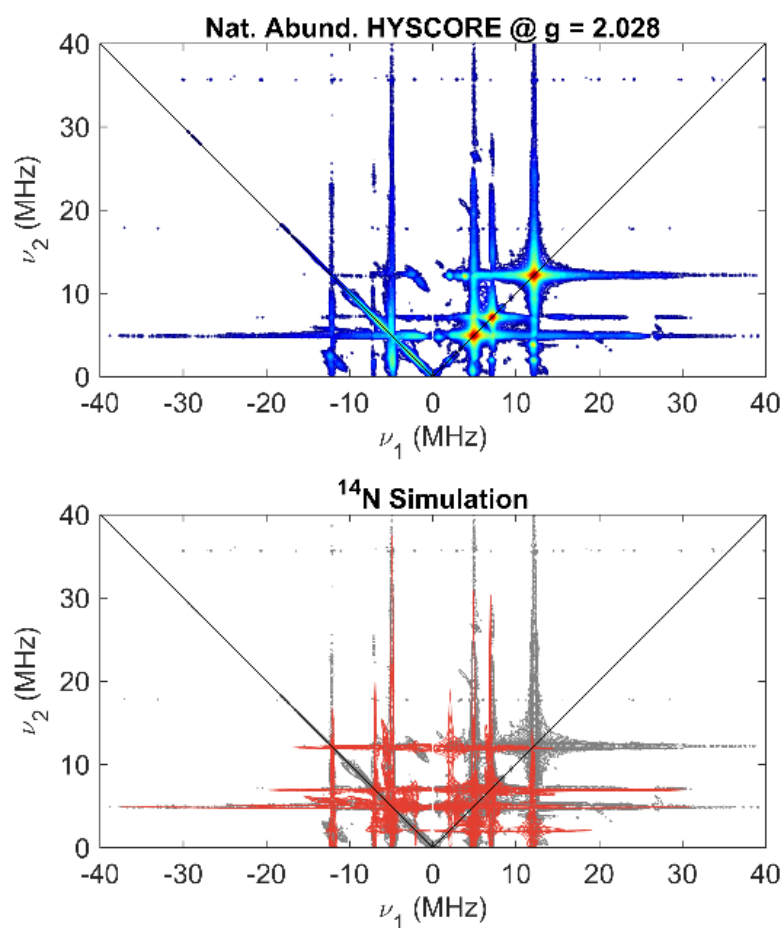


Figure S13. Top) Q-band HSCORE spectrum of natural abundance ($\text{P}_3^{\text{B}}\text{Fe}(\text{N})$ **4** acquired at 1201.5 mT ($g = 2.028$). Bottom) Simulation of ^{14}N HSCORE spectrum (red) overlaid over experimental data (grey) using parameters in Table 1 in the main text. Acquisition parameters: MW frequency = 34.103 GHz; temperature = 20 K; $\tau = 100$ ns, $t_1 = t_2 = 100$ ns; $\Delta t_1 = \Delta t_2 = 8$ ns; shot repetition time (srt) = 2 ms.

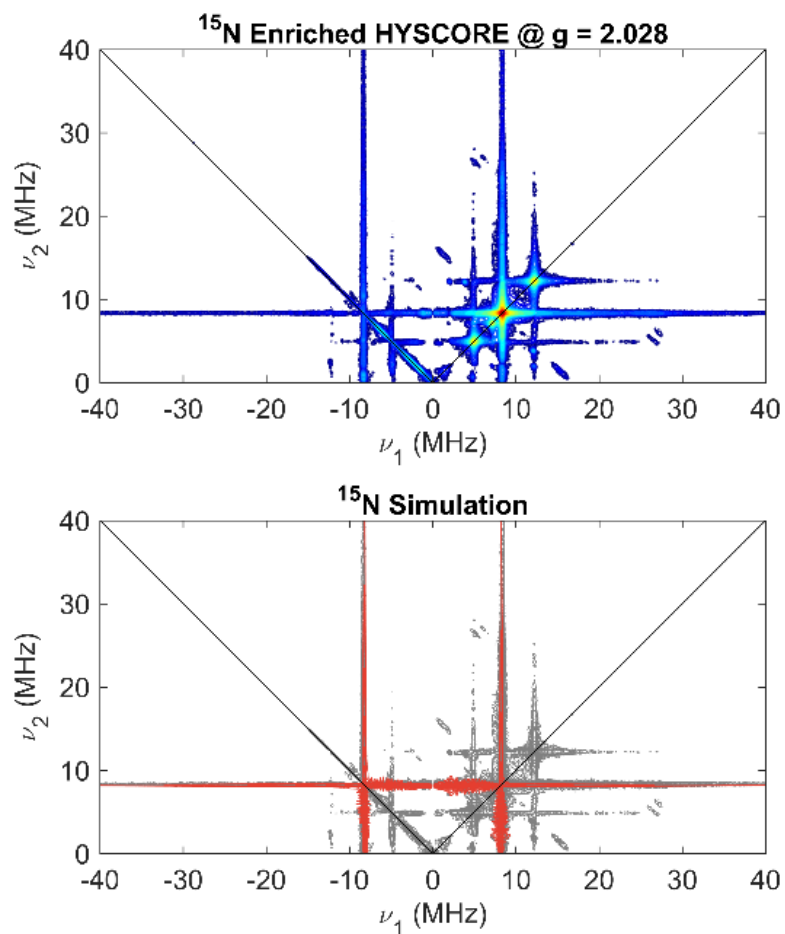


Figure S14. Top) Q-band HSCORE spectrum of ^{15}N enriched ($\sim 50\%$) $(\text{P}_3^{\text{B}})\text{Fe}(\text{N})$ acquired at 1201.5 mT ($g = 2.028$). Bottom) Simulation of ^{15}N HSCORE spectrum (red) overlaid over experimental data (grey) using parameters in Table 1 in the main text. Acquisition parameters: MW frequency = 34.103 GHz; temperature = 20 K; $\tau = 100$ ns, $t_1 = t_2 = 100$ ns; $\Delta t_1 = \Delta t_2 = 8$ ns; shot repetition time (srt) = 2 ms.

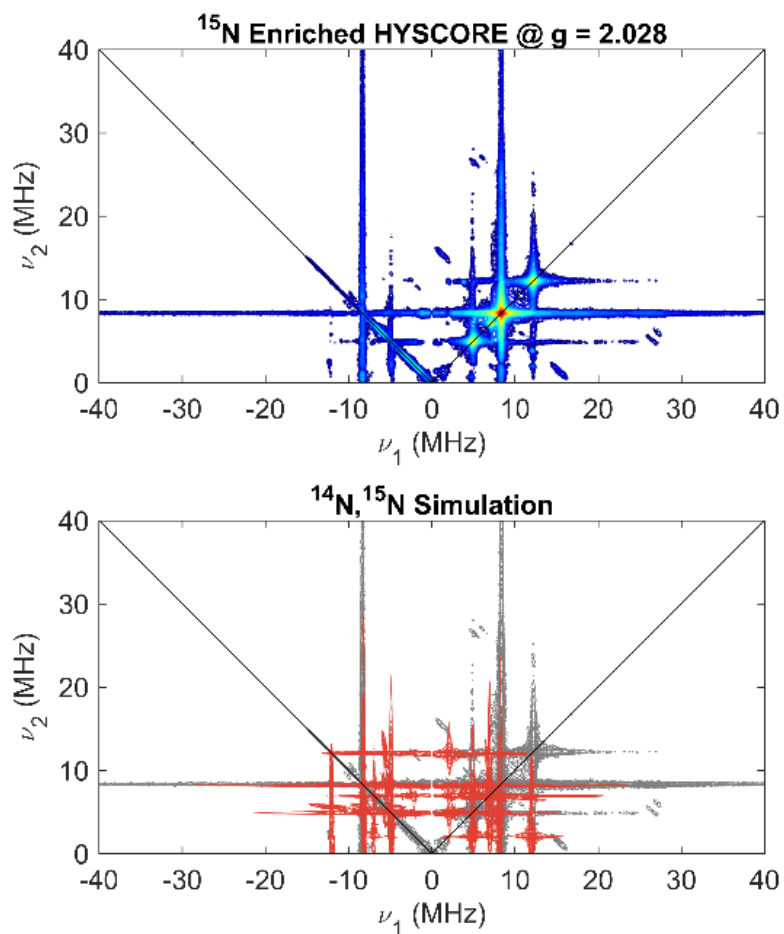


Figure S15. Top) Q-band Hyscore spectrum of ^{15}N enriched ($\sim 50\%$) $(\text{P}_3^{\text{B}})\text{Fe}(\text{N})$ acquired at 1201.5 mT ($g = 2.028$). Bottom) Simulation of both ^{14}N and ^{15}N contributions to Hyscore spectrum (red) overlaid over experimental data (grey) using parameters in Table 1 in the main text. Acquisition parameters: MW frequency = 34.103 GHz; temperature = 20 K; $\tau = 100$ ns, $t_1 = t_2 = 100$ ns; $\Delta t_1 = \Delta t_2 = 8$ ns; shot repetition time (srt) = 2 ms.

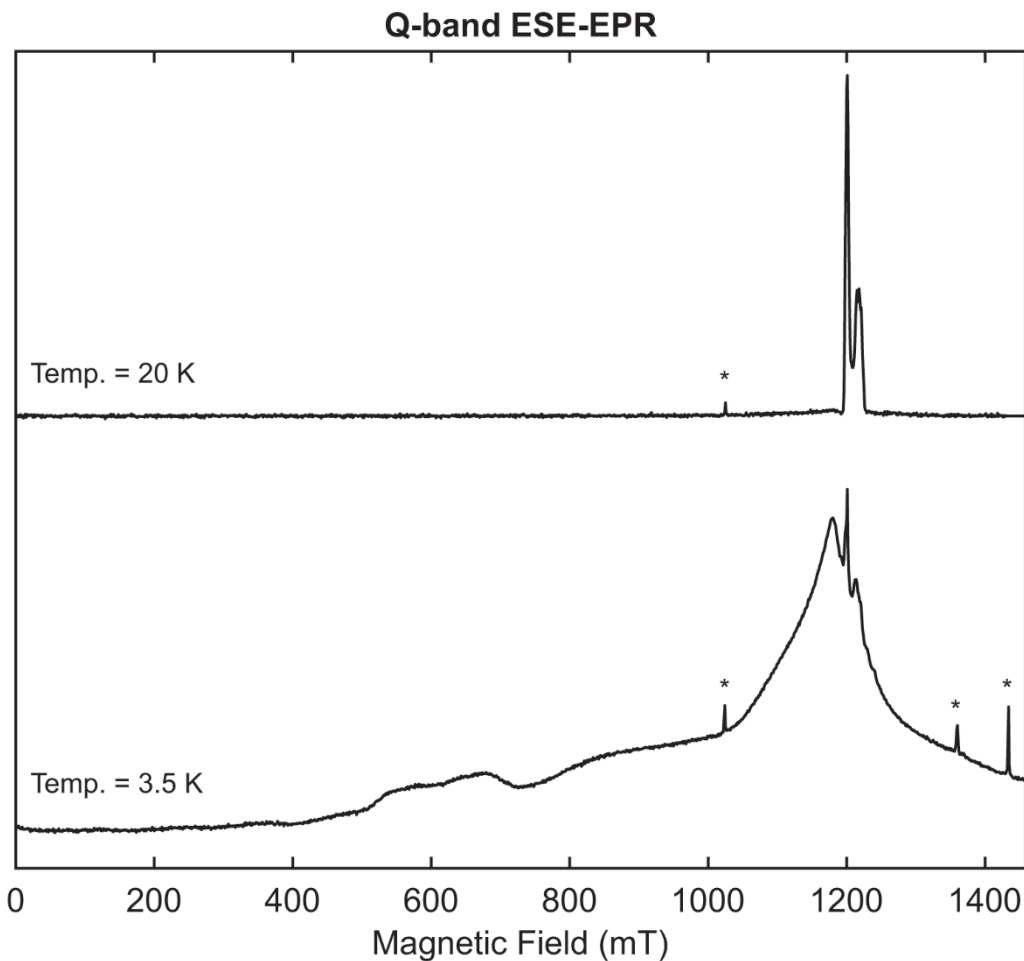


Figure S16. Comparison of Q-band ESE-EPR spectra collected at 20 K (top) and 3.5 K (bottom) of a frozen 2 mM solution of complex **2** ($\text{P}_3^{\text{B}}\text{Fe}(\text{N}_3)$) in 2-MeTHF after irradiation for 10 minutes, showing that the high-spin species generated during photolysis are observable at very low temperatures, but relax too fast to be observed at the temperature at which the pulse EPR measurements on **4** were performed. Asterisks indicate background signals arising from the Q-band resonator. Acquisition parameters: MW frequency = 34.071 GHz; π pulse length = 24 ns; τ = 200 ns; shot rep time (srt) = 1 ms.

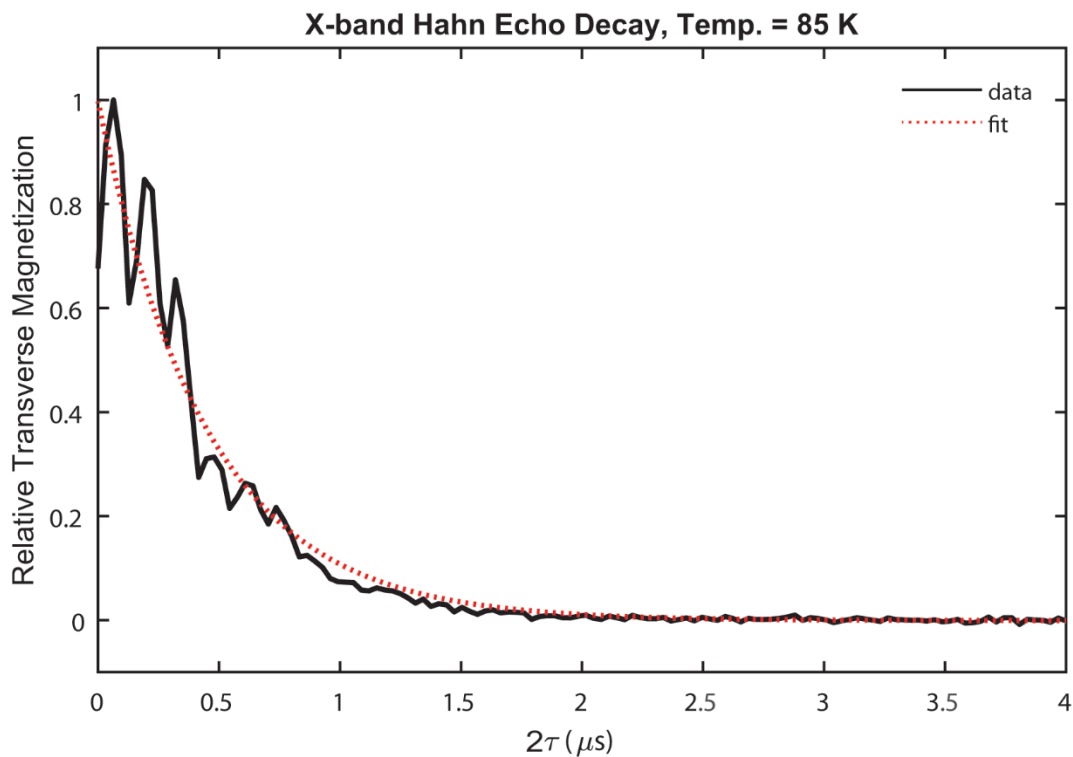


Figure S17. X-band Hahn-echo decay trace (black) collected at 337.1 mT ($g = 2.013$) at a temperature of 85 K with a fit (red) using a stretched exponential decay function.

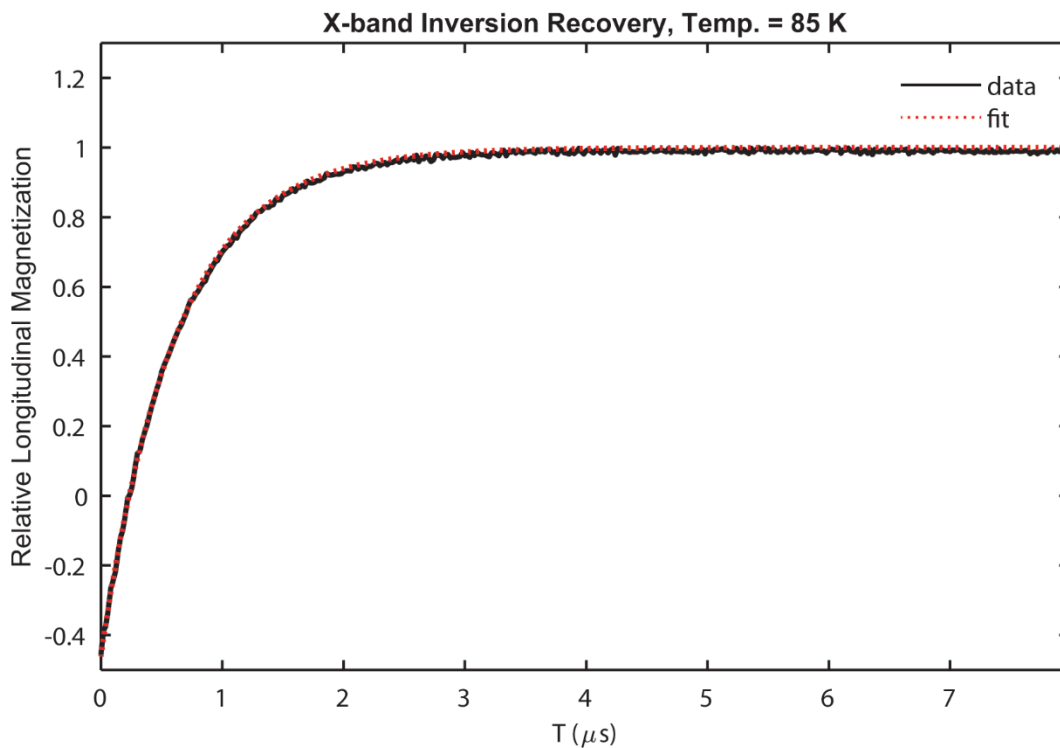


Figure S18. X-band inversion recovery trace of **4** (black) collected at 337.1 mT ($g = 2.013$) at a temperature of 85 K with a fit (red) using a stretched exponential decay function.

Table S1. T_1 and T_m relaxation times of **4** as determined by inversion recovery and Hahn-echo decay, respectively.

Temperature (K)	T_1 (μ s)	T_m (ns)
15	1067	992
30	32.4	952
50	3.82	736
85	0.62	262

5. Mössbauer Spectra

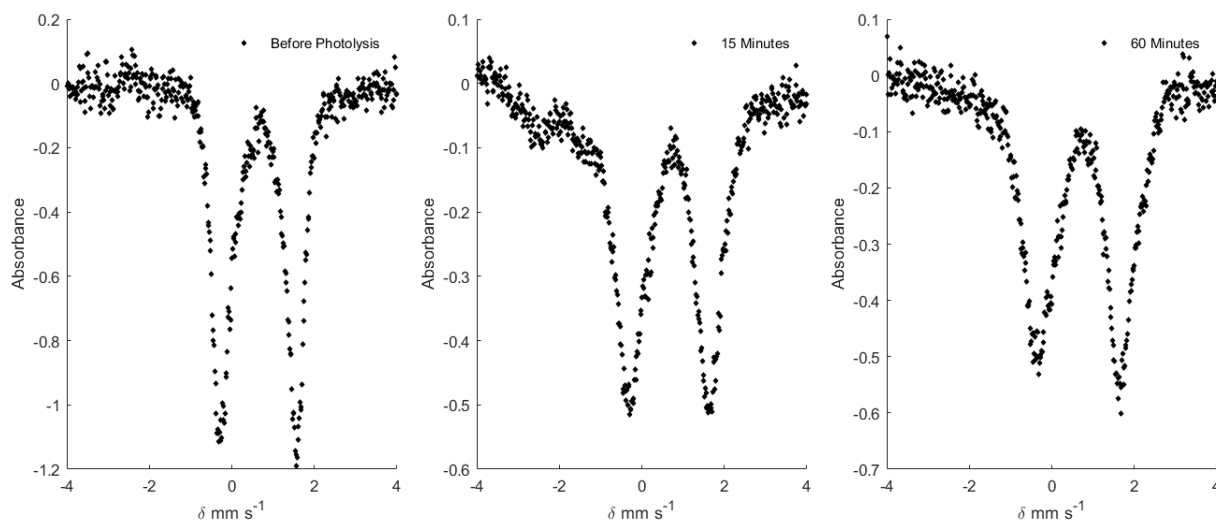


Figure S19. (left panel) Mössbauer spectrum at 80 K of azide precursor **2** before photolysis; (middle panel) after 15 minutes of photolysis, (right panel) after 60 minutes of photolysis. All photolysis was performed using a 40 W 390 nm LED.

6. UV-Vis Spectra

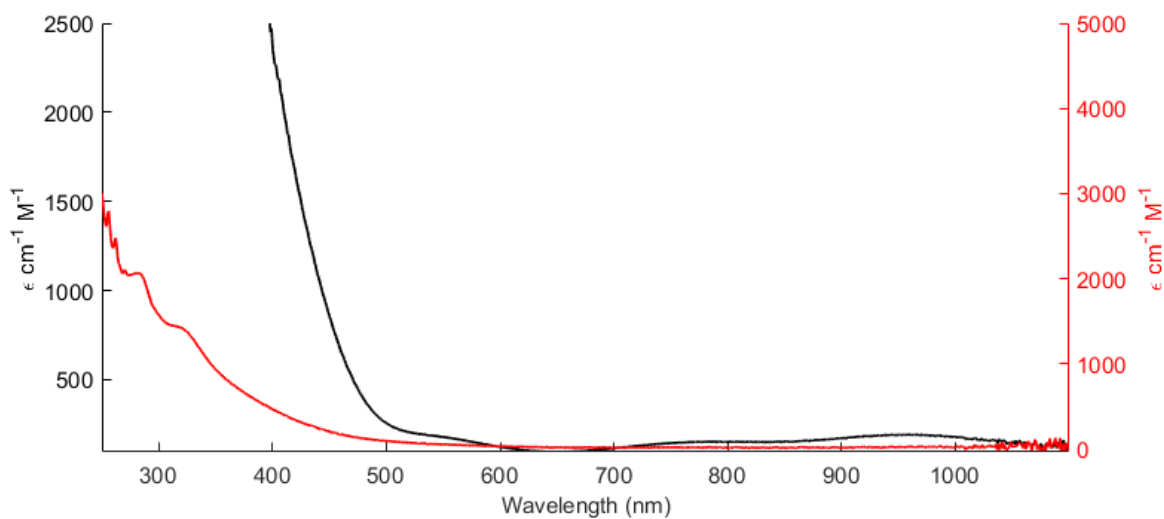


Figure S20. UV-visible spectrum of $(P_3^B)Fe(Cl)$ (**1**) (THF, 293 K). Black trace corresponds to the left axis scale, while the red trace corresponds to the right axis scale.

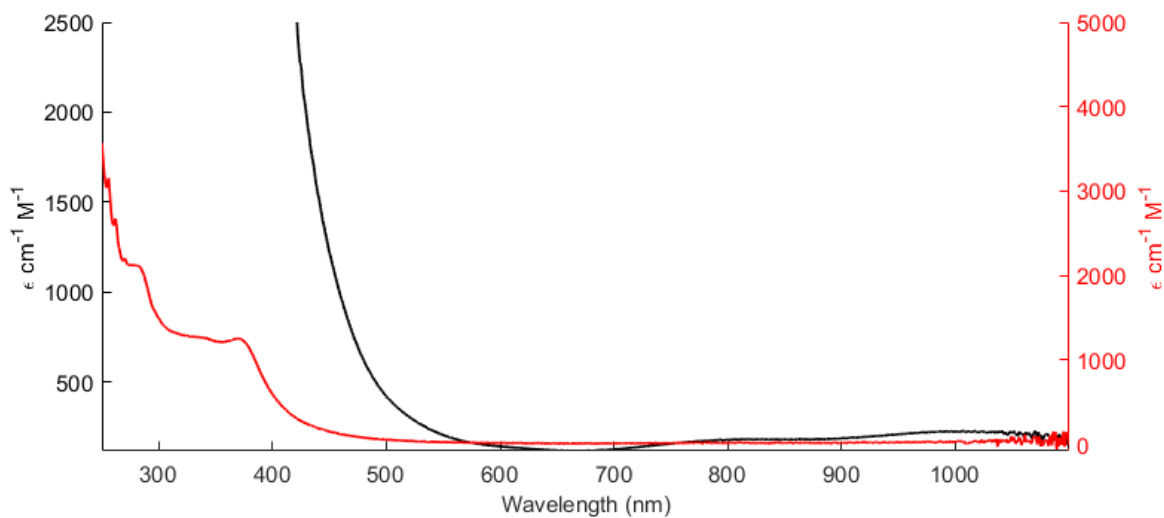


Figure S21. UV-visible spectrum of $(P_3^B)Fe(N_3)$ (**2**) (THF, 293 K). Black trace corresponds to the left axis scale, while the red trace corresponds to the right axis scale.

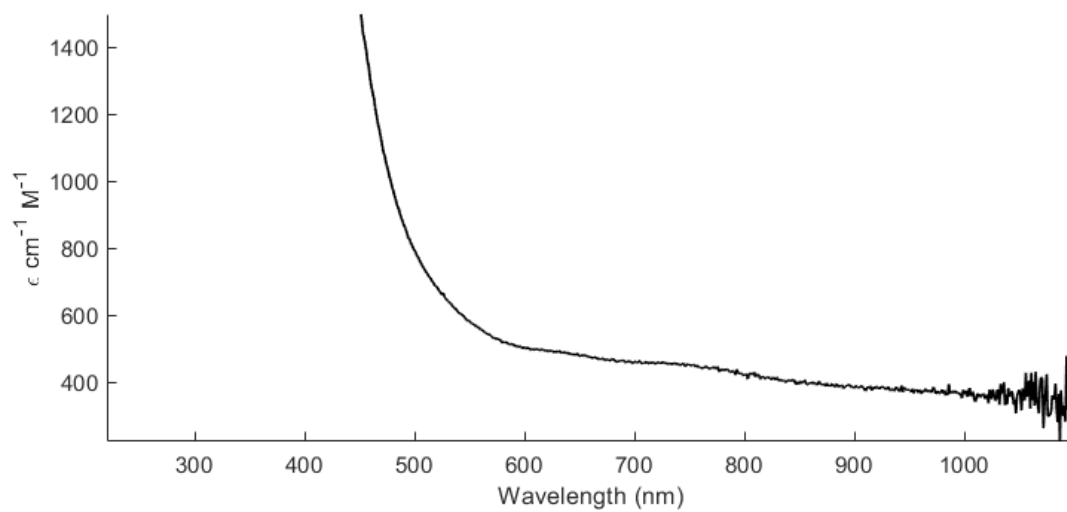


Figure S22. UV-visible spectrum $[(P_3^B)_2(\mu-1,3-N_3)]$ (**3**) generated *in-situ* by mixing equimolar solution of **2** and $(P_3^B)Fe(N_2)$ (THF, 293 K).

7. Crystallographic Details and Tables

Table S2. Crystallographic Data for Compounds **1-3**

	1	2	3
chem formula	C ₃₆ H ₅₄ BClFeP ₃	C _{38.5} H ₆₀ BFeN ₃ P ₃	C ₈₄ H ₁₂₀ B ₂ Fe ₂ N ₃ P ₆
fw	681.81	724.47	1490.96
cryst syst	Triclinic	Cubic	Monoclinic
space group	P-1	Pa-3	P21/c
a [Å]	10.8929(7)	19.953(3)	11.0614(7)
b [Å]	11.5482(7)	19.953(3)	17.7504(11)
c [Å]	15.8266(9)	19.953(3)	20.8069(12)
α [°]	91.335(2)	90	90
β [°]	97.048(2)	90	102.344(3)
γ [°]	117.325(2)	90	90
V [Å ³]	1748.20(19)	7944(4)	3990.9(4)
Z	2	8	2
Dcalcd [g cm ⁻³]	1.295	1.211	1.241
F(000)	726	3107.4	1594
μ [mm ⁻¹]	0.670	0.53	0.529
temp. [K]	100	100	100
wavelength [Å]	0.71073	0.71073	0.71073
measd rflns	104461	156002	41848
unique rflns	21944	8697	8148
data/restraints/param	21944/6/417	8697/68/182	8148/300/451
R(F) (<i>I</i> >2σ(<i>I</i>))	0.0363	0.0379	0.0581
wR(F ²) (all)	0.0942	0.1101	0.1286
GOF	1.022	1.080	1.017

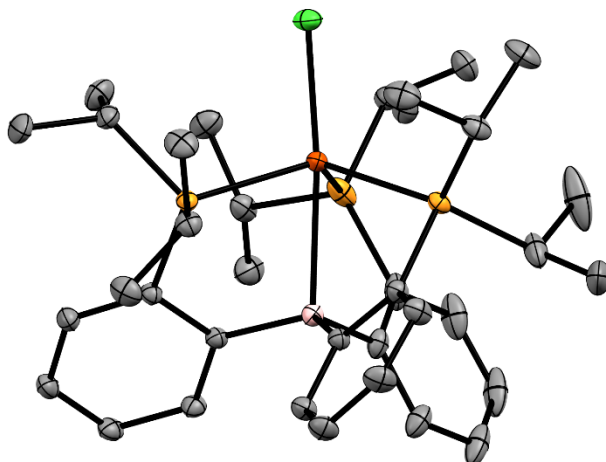


Figure S23. Thermal ellipsoid plot of **1** (50%, hydrogens omitted for clarity).

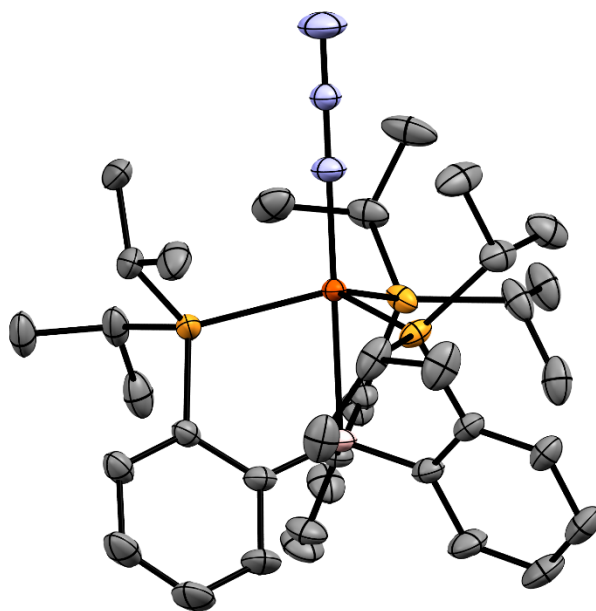


Figure S24. Thermal ellipsoid plot of **2** (50%, hydrogens omitted for clarity).

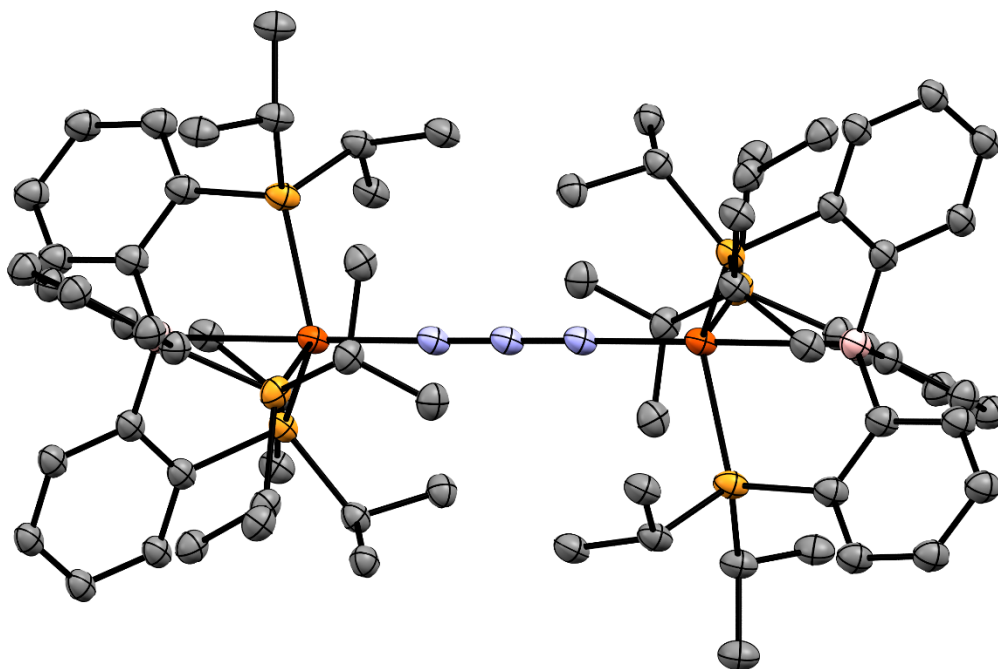


Figure S25. Thermal ellipsoid plot of **3** (50%, hydrogens and solvent molecule omitted for clarity).

8. DFT Calculations

8.1 General:

All calculations were performed using the ORCA 4.0⁵⁻⁷ program. In cases where crystal structures were available these coordinates were used as the input. The calculations were performed using the TPSS (meta-GGA)⁸ functional with the def2-SVP basis set was on C and H and the def2-TZVP basis set on Fe. To assure that optimized structures represented true stationary points was checked by doing a single-point frequency calculations on the optimized structure.

EPR parameters were calculated using, TPPSh, TPSS, B3LYP, M06L and BP86 with for the TPSS-optimized structure were calculated by doing a single point calculation on the optimized structures using CP(PPP)⁹ on Fe and IGLO-III¹⁰ on everything else grid 7. These basis sets and functionals have previously shown to be good predictors of phosphine and hydrogen hyperfine coupling constants in iron phosphine complexes.^{11,12} See below for a summary of the results.

8.2 EPR predictions

Table S3. Experimental and DFT-calculated EPR parameters. Experimental $g = [2.0293, 2.0293, 1.9975]$. All hyperfine and nuclear quadrupole coupling constants reported in units of MHz.

Functional	Basis set	$a_{\text{iso}}(^{14}\text{N})$	$A(^{14}\text{N})$	$\frac{e^2Qq}{h}$ (^{14}N)	η (^{14}N)	$a_{\text{iso}}(^{11}\text{B})$	$A(^{11}\text{B})$	$\frac{e^2Qq}{h}$ (^{11}B)	η (^{11}B)	$a_{\text{iso}}(^{31}\text{P})$	$A(^{31}\text{P})$	$a_{\text{iso}}(^{57}\text{Fe})$	$A(^{57}\text{Fe})$
experimental		± 3.9	$\pm [-4.3, -4.3, 20.3]$	$\approx \pm 3.1$	≈ 0	± 41.3	$\pm [21.5, 21.5, 81.0]$	$\approx \pm 2.8$	≈ 0	± 44.3	$\pm [49, 45, 39]$	± 22	$\pm [10.5, 10.5, 46.0]$
TPSS	IGLO-III	1.62	[-8.0, -8.0, 20.87]	-3.08	0.001	40.1	[20.3, 20.3, 79.7]	2.78	0.003	-33.5	[-28.7, -33.5, -38.3]	19.4	[9.2, 9.3, 39.7]
TPSSh	IGLO-III	1.9	[-7.7, -7.8, 21.2]			40.1	[20.3, 20.3, 79.7]			-40.4	[-35.5, -39.8, -45.8]	21.8	[11.3, 11.3, 42.7]
B3LYP	IGLO-III	3.6	[-4.8, -4.8, 20.5]			39.0	[18.0, 18.0, 81.0]			-38.5	[-33.6, 38.2, 43.6]	21.9	[10.5, 10.6, 44.6]
BP86	IGLO-III	-0.26	[-9.0, -9.0, 17.3]			34.23	[13.8, 13.8, 75.1]			-35.4	[-30.2, -35.6, -0.51]	16.75	[6.5, 6.5, 37.2]
M06l	IGLO-III	3.52	[-11.6, -11.7, 33.9]			25.0	[2.3, 2.8, 69.8]			-59.0	[-52.4, -59.4, 65.1]	20.5	[10.1, 10.2, 41.1]

9. References:

- (1) Bontemps, S.; Bouhadir, G.; Dyer, P. W.; Miqueu, K.; Bourissou, D. Quasi-Thermoneutral P → B Interactions within Di- and Tri-Phosphine Boranes. *Inorg. Chem.* **2007**, *46* (13), 5149–5151.
- (2) Moret, M.-E.; Peters, J. C. Terminal Iron Dinitrogen and Iron Imide Complexes Supported by a Tris(Phosphino)Borane Ligand. *Angew. Chem. Int. Ed.* **2011**, *50*, 2063–2067.
- (3) Anderson, J. S.; Moret, M. E.; Peters, J. C. Conversion of Fe–NH₂ to Fe–N₂ with Release of NH₃. *J. Am. Chem. Soc.* **2013**, *135* (2), 534–537.
- (4) Ayscough, P. B.; Thomson, C. Electron Spin Resonance Spectra of Alkyl Radicals in γ -Irradiated Alkyl Halides. *Trans. Faraday Soc.* **1962**, *58* (0), 1477–1494.
- (5) Stoll, S.; Schweiger, A. EasySpin, a comprehensive software package for spectral simulation and analysis in EPR *Journal of Magnetic Resonance*, **2006**, *178*, 42–55.
- (6) Neese, F. The ORCA Program System. *WIREs Computational Molecular Science* **2012**, *2* (1), 73–78.
- (7) Neese, F. Software Update: The ORCA Program System, Version 4.0. *WIREs Computational Molecular Science* **2018**, *8* (1), e1327.
- (8) Tao, J.; Perdew, J. P.; Staroverov, V. N.; Scuseria, G. E. Climbing the Density Functional Ladder: Nonempirical Meta-Generalized Gradient Approximation Designed for Molecules and Solids. *Phys. Rev. Lett.* **2003**, *91* (14), 146401–146404.
- (9) Neese, F. Prediction and Interpretation of the ⁵⁷Fe Isomer Shift in Mössbauer Spectra by Density Functional Theory. *Inorganica Chimica Acta* **2002**, *337*, 181–192.
- (10) Kutzelnigg, W.; Fleischer, U.; Schindler, M. The IGLO-Method: Ab-Initio Calculation and Interpretation of NMR Chemical Shifts and Magnetic Susceptibilities. In *Deuterium and Shift Calculation*; Fleischer, U., Kutzelnigg, W., Limbach, H.-H., Martin, G. J., Martin, M. L., Schindler, M., Eds.; Springer Berlin Heidelberg: Berlin, Heidelberg, 1991; pp 165–262.
- (11) Drover, M. W.; Schild, D. J.; Oyala, P. H.; Peters, J. C. Snapshots of a Migrating H-Atom: Characterization of a Reactive Iron(III) Indenide Hydride and Its Nearly Isoenergetic Ring-Protonated Iron(I) Isomer. *Angewandte Chemie International Edition* **2019**, *58* (43), 15504–15511.
- (12) Schild, D. J.; Drover, M. W.; Oyala, P. H.; Peters, J. C. Generating Potent C–H PCET Donors: Ligand-Induced Fe-to-Ring Proton Migration from a Cp*Fe^{III}–H Complex Demonstrates a Promising Strategy. *J. Am. Chem. Soc.* **2020**, *142* (44), 18963–18970.